A predictive, size-dependent continuum model for dense granular flows

A predictive, size-dependent continuum model for dense granular flows

David L. Henann and Ken Kamrin[1]

Department of Mechanical Engineering, Massachusetts Institute of Technology, Cambridge, MA 02139

Edited* by James S. Langer, University of California, Santa Barbara, CA, and approved February 20, 2013 (received for review November 2, 2012)

Dense granular materials display a complicated set of flow properties, which differentiate them from ordinary fluids. Despite their ubiquity, no model has been developed that captures or predicts the complexities of granular flow, posing an obstacle in industrial and geophysical applications. Here we propose a 3D constitutive model for well-developed, dense granular flows aimed at filling this need. The key ingredient of the theory is a grain-size-dependent nonlocal rheology—inspired by efforts for emulsions—in which flow at a point is affected by the local stress as well as the flow in neighboring material. The microscopic physical basis for this approach borrows from recent principles in soft glassy rheology. The size-dependence is captured using a single material parameter, and the resulting model is able to quantitatively describe dense granular flows in an array of different geometries. Of particular importance, it passes the stringent test of capturing all aspects of the highly nontrivial flows observed in split-bottom cells—a geometry that has resisted modeling efforts for nearly a decade. A key benefit of the model is its simple-to-implement and highly predictive final form, as needed for many real-world applications.

Granular materials are ubiquitous in day-to-day life, as well as central to important industries, such as geotechnical, energy, pharmaceutical, and food processing. In fact, granular matter is second only to water as the most handled industrial material (1), but unlike water, dense granular flows are substantially more complex (2–10). In particular, slowly flowing granular media form clear, experimentally robust features, most notably, shear bands, which can have a variety of possible widths and decay nontrivially into the surrounding quasi-rigid material. However, these behaviors remain poorly understood and have not been rationalized with a universal continuum model, posing a costly problem in industry. Quantitatively describing and predicting dense, well-developed granular flows with a constitutive model that may be applied in arbitrary configurations remains a major open challenge.

For many years, mechanicians and materials engineers have approached granular materials modeling from a soil mechanics perspective, grounded in the principles of continuum solid mechanics, invoking various yield criteria and plastic flow relations (11, 12). In contrast, over the past two decades, a resurgence of interest in granular media has arisen among physicists, primarily drawing upon statistical and fluid dynamical approaches (13, 14). More recently, drawing upon both schools of thought, granular rheologists have made progress combining a fluid-like, rate-dependent flow approach with an appropriate yield criterion. Backed by numerous experiments and a coherent dimensional argument, the key result is the dimensionless relation $\mu = \mu(I)$, consistent with the seminal work of Bagnold (15), which has become a well-regarded basis for modeling well-developed granular flows in simple shear (9, 16), where $\mu = \tau/P$ for shear stress τ and normal pressure P, and $I = \dot{\gamma}\sqrt{d^2\rho_s/P}$ is the inertial number for shear strain-rate $\dot{\gamma}$, grain diameter d, and grain density ρ_s. The inertial number operates as a normalized shear rate and represents the ratio of the macroscopic time of applied deformation to the microscopic time of the particle motion.

The relation $\mu = \mu(I)$ may be inverted and expressed as a strain-rate formula. Empirical fits to numerical experiments (16) indicate the result is Bingham-like,

$$\dot{\gamma} = \dot{\gamma}_{\mathrm{loc}}(P,\mu) = \begin{cases} \sqrt{P/\rho_s d^2}\ (\mu-\mu_s)/b & \text{if} \quad \mu > \mu_s, \\ 0 & \text{if} \quad \mu \le \mu_s, \end{cases} \qquad [1]$$

for dimensionless constant b and static yield value μ_s. We refer to $\dot{\gamma}_{\mathrm{loc}}(P,\mu)$ as the local rheology because it directly relates the local stress state to the local state of strain rate. The above may be extended to three dimensions by presuming incompressibility and codirectionality of the strain rate and Cauchy stress tensors (17, 18).

The 3D version has had success in describing both uniform and fast ($10^{-3} \lesssim I \lesssim 10^{-1}$), dense flows; however, problems arise for slow ($I \lesssim 10^{-3}$), nonuniform flows. Under these circumstances, the one-to-one $\mu = \mu(I)$ relation is violated (19), and the local rheology gives poor flow predictions (20). Specifically, contrary to Eq. **1**, flow is observed for $\mu < \mu_s$ in the presence of a strain-rate gradient (19). Whereas the local model predicts a sharp flow cutoff to occur where $\mu = \mu_s$, an exponential-type decay profile, scaled by the particle size, is typically observed in the quasi-static region where $\mu < \mu_s$ (3, 8–10, 19, 21, 22). Moreover, a strongly flow-rate-independent stress response emerges where $\mu < \mu_s$ in a fashion inconsistent with Eq. **1**. (9, 19, 21, 22). These flow features are signatures of finite-size effects, arising due to a finite grain size compared with that of the flow environment.

Motivated by these shortcomings, significant effort has gone into developing physically nonlocal models for granular flow. Approaches include integral equations representing a self-activated process (23), theories of partial fluidization governed by a Ginzberg–Landau order parameter (24), Cosserat plasticity-based models (25), extensions of kinetic theory to the slow-flow regime (26, 27), and the stochastic flow rule (28). Each of these models displays a "diffusive" character—although invoking different physical hypotheses, each accomplishes the essential qualitative goal of spreading sharply varying flow features on the basis of grain size. This notion has been understood for decades to be an important missing piece in granular flow modeling (29, 30). What ultimately distinguishes such models, hence, are the details of the diffusive process that is claimed to be underlying the flow. Specifically, models differ on (*i*) the physical meaning and mathematical form of the variable responsible for diffusion, (*ii*) the details of the differential or integral system it must satisfy, and (*iii*) how it couples to the mechanics to influence the flow. Despite the various models tried, none of the aforementioned approaches have been able to demonstrate quantitative predictivity in arbitrary geometries.

Recently, finite-size effects in emulsions and bubble rafts have been addressed using the concept of size-dependent fluidity (inverse viscosity) (31–33), which introduces a nonlocal term involving a microscopic length scale. Analogously, the "granular fluidity" g may be introduced and defined as $g = \dot{\gamma}/\mu$, relating the shear flow rate $\dot{\gamma}$ to what drives the flow, which for a granular

Author contributions: D.L.H. and K.K. designed research; D.L.H. and K.K. performed research; D.L.H. analyzed data; and D.L.H. and K.K. wrote the paper.

The authors declare no conflict of interest.

*This Direct Submission article had a prearranged editor.

[1]To whom correspondence should be addressed. E-mail: kkamrin@mit.edu.

This article contains supporting information online at www.pnas.org/lookup/suppl/doi:10.1073/pnas.1219153110/-/DCSupplemental.

material is μ. Recent work (21), using 2D discrete-element method (DEM) simulations in several different geometries, indicated that g satisfies a universal grain-size-dependent differential relation roughly analogous to that observed for emulsions (32). The relation accounts for the observed loss of uniqueness in the relation between μ and I (19), while collapsing to the local law in uniform flows.

On the basis of these observations, in this work, we propose a continuum-level, 3D constitutive system for well-developed granular flow. Our model builds in the successes of the local rheology, but extends the range of applicability to $I \lesssim 10^{-3}$ through the introduction a differential relation for the granular fluidity, enabling an accounting of size effects. Following similar assumptions to those of the local rheology, we consider grains that are (*i*) spherical, (*ii*) quasi-monodisperse, and (*iii*) stiff enough so that the wave speed is much greater than the deformation speed. In addition to the material parameters of the local rheology, μ_s and b, we introduce a single dimensionless parameter, A, the nonlocal amplitude, which characterizes the cooperativity of flow. Upon calibrating this parameter, the model predictions match numerous experimental flows of glass beads in multiple families of geometries, including the split-bottom family (4–6), whose flow fields have until now resisted continuum description. Our approach has the joint benefits of being based on physically grounded microscopic arguments, while being straightforward enough for tractable numerical implementation in arbitrary geometries and carrying demonstrable predictivity among a variety of test cases.

Continuum Model

Define the strain-rate tensor as $\dot{\gamma}_{ij} = (\partial v_i/\partial x_j + \partial v_j/\partial x_i)/2$, where v_i is the velocity field and x_i is the spatial coordinate, and the Cauchy stress tensor is $\sigma_{ij} = \sigma_{ji}$. Define the strain-rate deviator as $\dot{\gamma}'_{ij} = \dot{\gamma}_{ij} - (1/3)(\dot{\gamma}_{kk})\delta_{ij}$ and the stress deviator σ'_{ij} similarly. The equivalent shear stress and equivalent shear rate are defined, respectively, by $\tau = (\sigma'_{ij}\sigma'_{ij}/2)^{1/2}$ and $\dot{\gamma} = (2\dot{\gamma}'_{ij}\dot{\gamma}'_{ij})^{1/2}$, and we use the spherical pressure $P = -\sigma_{kk}/3$. The ratio $\mu = \tau/P$ is now the Drucker–Prager stress ratio, which we adopt along with $g = \dot{\gamma}/\mu$.

It has been observed in DEM simulations of multiple nonuniform, well-developed slow-flow environments (19, 34) that, unlike the μ vs. I relationship, a relatively predictable, one-to-one dependence of the packing fraction ϕ on the pressure P and shearing rate $\dot{\gamma}$ emerges, which may be expressed as $\phi = \phi(I)$, indicating that steady flow progresses at constant volume, i.e., $\dot{\gamma}_{kk} = 0$, which we shall adopt. This is a common assumption in well-developed granular flow modeling (17, 18, 23–25, 28), providing considerable simplification, while generally still providing good steady-flow predictions in a wide variety of environments.

With these definitions, the stress is given by

$$\sigma_{ij} = -P\delta_{ij} + 2\frac{P}{g}\dot{\gamma}_{ij}. \qquad [2]$$

Implicit in Eq. **2** is that the tensorial directions of σ_{ij} and $\dot{\gamma}_{ij}$ are related through codirectionality (19, 34). We propose that the granular fluidity g is governed by the differential relation

$$\nabla^2 g = \frac{1}{\xi^2}(g - g_{\mathrm{loc}}), \qquad [3]$$

where $g_{\mathrm{loc}} = \dot{\gamma}_{\mathrm{loc}}(P,\mu)/\mu$ is the local granular fluidity, with $\dot{\gamma}_{\mathrm{loc}}(P,\mu)$ given by Eq. **1**, and ξ is the cooperativity length for plastic rearrangement, which is directly proportional to d, thereby imposing a length scale on the flow. Note that in the absence of any stress or flow gradients, the system reduces to the local law as it should. Where the local law has no contribution (i.e., $g_{\mathrm{loc}} = 0$, $\mu < \mu_s$), the differential relation Eq. **3** becomes a linear equation whose solutions can always be scaled by a constant. This gives precisely the slow-flow, rate-independent effect observed. And due to the Laplacian term, flow naturally spreads near μ_s with a decay determined by ξ, instead of a sharp flow cutoff.

The physical basis of Eq. **3**, as derived mathematically for the viscoplastic behavior of pressure-insensitive amorphous materials with interest in emulsions (31), is based on the statistics of a kinetic elasto-plastic (KEP) mechanism. The microscopic picture behind the KEP mechanism is similar to that of soft glassy rheology (SGR) (35) with a few key differences. Like SGR, the KEP mechanism envisions mesoscopic regions of material that may undergo local elastic loading as well as plastic yielding and subsequent relaxation to a new local equilibrium position. Unlike SGR, yielding events are not assumed to be "thermally activated" by an effective "noise temperature." In fact, the interactions between mesoscopic regions are explicitly accounted for by positing that localized yield events induce elastic modifications in nearby regions, leading to a highly cooperative picture of flow. Invoking this microscopic description, a continuum-level differential relation in the same vein as Eq. **3** is derived. It is this notion of cooperativity, i.e., flow inducing flow, that directly leads to its differential nature. Other nonlocal models stem from a similar microscopic picture (23, 36, 37).

Instead of rederiving the KEP mechanism here for dry grains, we adapt its final result for pressure-insensitive emulsions to our purposes by using the pressure-dependent granular fluidity g. The microscopic picture for this mechanism as applied to a granular material may be imagined as follows. A localized zone of plastic grain rearrangement produces nonlocal elastic stress fluctuations extending $\sim\xi$ away from the zone. These fluctuations superpose with the stresses due to applied loads and can cause a neighboring material element to flow when otherwise it would not. Consequently, g, the relative susceptibility to flow in a granular medium, has a contribution due to the local stress (g_{loc}) and one connecting to how much neighboring material is moving ($\xi^2\nabla^2 g$).

Importantly, the statistical argument (31) concludes that ξ is not a constant, but in fact a specific function of the local stress. We have adopted a similar functional form, using μ as the stress variable as appropriate for a granular material,

$$\xi(\mu) = \frac{A}{\sqrt{|\mu - \mu_s|}}d, \qquad [4]$$

with A a dimensionless constant, the nonlocal amplitude, characterizing the cooperativity of flow. The functional form of Eq. **4** is consistent with past work on length-scale effects in amorphous materials (36–40) in that it diverges at a yield (or jamming) point; however, the precise definition of the length scale as well as the nature of the power-law divergence varies among these studies. Our approach of taking ξ to diverge in μ with the $-1/2$ power law of Eq. **4** is consistent with the KEP argument (31) and, from a pragmatic perspective, provides the best description of experimental data. (See *SI Text* and Fig. S1 for an expanded discussion.) We emphasize that the divergence of ξ at μ_s does not affect the well-behaved nature of Eq. **3**. The nonlocal amplitude A is directly connected to the "elastic stress propagator" in the KEP mechanism, which describes the precise form of nonlocal stress fluctuations in nearby material due to yielding events. Conceivably, A may be estimated from the explicit form of this microscopic operator; however, in the present work, it is much simpler to observe its value from flow data.

The system is closed mathematically by the usual equations of motion, $\partial\sigma_{ij}/\partial x_j + \phi\rho_s G_i = \phi\rho_s\dot{v}_i$, for G_i the acceleration of gravity and ϕ the packing fraction, which we take here to be near random close packing $\phi = 0.62$ for quasi-monodisperse spherical grains. To implement the system numerically, we have custom-written a User Element within the Abaqus finite-element package (41), which calculates g as an added degree of freedom coupled to the stress/kinematic variables. We have developed a 3D continuum brick element and model all subsequently described problems in three dimensions. For ease, we also neglect macroscopic inertial effects ($\phi\rho_s\dot{v}_i \approx 0$) due to our current interest in

steady, slow-flow phenomena; however, it is straightforward to include these effects if necessary for rapid flows. (See *Materials and Methods* and *SI Text* for further discussion of our finite-element method procedures.) For the fluidity boundary conditions, throughout this work, we assume the simplest, least disruptive case: $n_i(\partial g/\partial x_i) = 0$ for n_i the surface normal. (See *SI Text* for further discussion of the granular fluidity boundary conditions.)

Numerical Solutions

Flows in the Split-Bottom Geometry—Shallow Layers. We first turn attention to flows in the split-bottom geometry, pictured in Fig. 1*A*. The geometry is an annular cell with fully rough walls at inner radius R_i and outer radius R_o and an open top, having a bottom that is split at some radius R_s. It is filled with grains to a height H, and the outer portion (gray in Fig. 1*A*) is then rotated at a rate Ω, holding the center portion (blue in Fig. 1*A*) stationary. The geometry was introduced by Fenistein and van Hecke (4), and its flow features and wide shear bands have challenged granular materials researchers for much of the last decade, becoming the subject of many papers (5–7, 20, 42–47). No continuum model has successfully described split-bottom flows (47). In fact, all local constitutive relations are intrinsically insufficient, predicting an infinitely sharp shear band for slow steady Ω (20, 42), whereas the observed flow is always smooth with a wide shear zone (4). Following the experiments, we focus on matter composed of quasi-monodisperse spherical glass beads. The local relation parameters for glass beads are taken from existing simple shear data (48): $\mu_s = 0.3819$, $b = 0.9377$, and $\rho_s = 2{,}450$ kg/m^3. By fitting to the experimental data for shallow flows in the split-bottom cell, we take $A = 0.48$ and use this value throughout the paper. We emphasize that A is the only model parameter that was not known in advance.

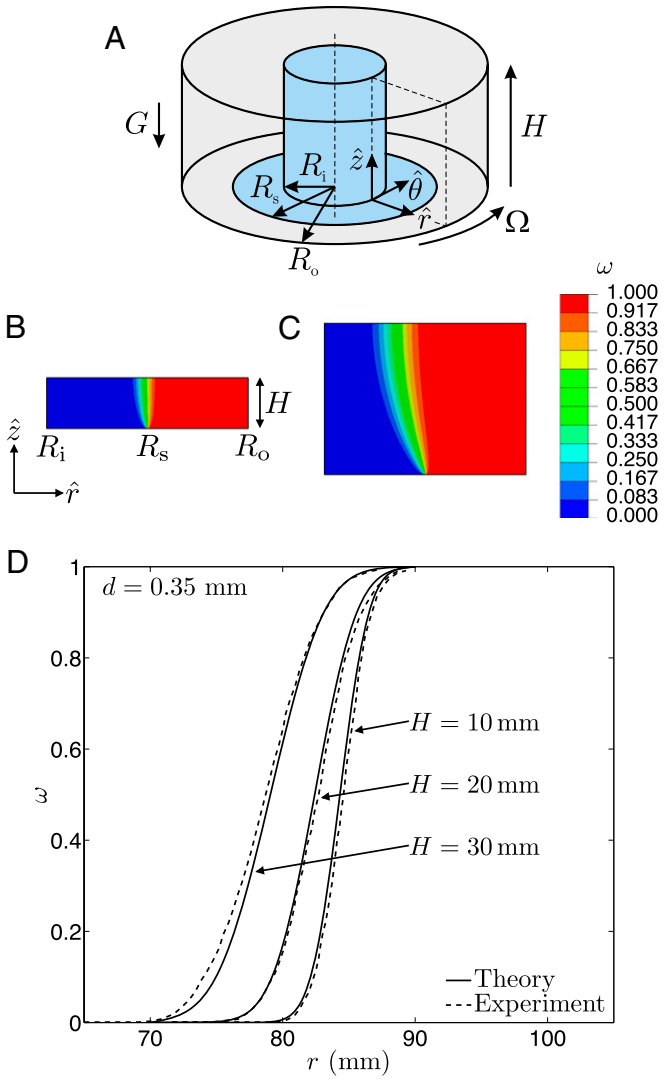

Fig. 1. Flows in the split-bottom geometry. (*A*) Schematic of the split-bottom geometry. The blue inner section is fixed, while the gray outer section rotates. The side walls and bottom are rough, whereas the top is open. (*B* and *C*) Theoretical flow profiles in the *r*-*z* plane for (*B*) $H = 10$ mm and (*C*) $H = 30$ mm with $R_s = 85$ mm and $d = 0.35$ mm. (*D*) Comparison of surface flows to experimental data (4) for $H = 10$, 20, and 30 mm.

We first simulate shallow layers in the split-bottom cell on the basis of the configurational parameters used in experiments (4, 5), taking $R_i = 65$ mm, $R_s = 85$ mm, $R_o = 105$ mm, and $\Omega = 0.16$ rad/s. We consider four particle sizes $d = 0.35$, 0.8, 1.2, and 2.2 mm, which are taken to be representative of the four quasi-monodisperse mixtures of spherical glass beads used in experiments (5), and a variety of filling heights H, ranging between 5 mm and 35 mm. We neglect combinations of H and d for which $H/d < 5$ as well as higher values of H in which the shear band region localizes to the inner wall, which is beyond the scope of interest here (but included in Fig. S2). In total, we consider 22 combinations. (See *Materials and Methods* for further simulation details.)

For each combination of H and d, we calculate the steady-state flow predictions. We introduce the quantity $\omega = v_\theta/r\Omega$, referred to as the normalized revolution rate, which varies from 0 (static) to 1 (rotating at Ω). To demonstrate typical calculated flow fields, contour plots of ω at steady state in the *r*-*z* plane are shown in Fig. 1 *B* and *C* for $d = 0.35$ mm and $H = 10$ and 30 mm, respectively. A shear band is clearly observable, emanating from the split along the bottom of the cell. The shear band gradually moves inward toward the inner wall with increasing height, accompanied by a broadening of the shear-band width before terminating at the top surface. For the purpose of comparing to experiments, we introduce the surface flow, defined as $\omega(r, z = H)$. Fig. 1*D* displays the excellent quantitative agreement between the predictions of the theory and experimental data of surface flows for $d = 0.35$ mm and $H = 10$, 20, and 30 mm.

Importantly, van Hecke and coworkers (4, 5) have shown that the dependence of ω on r along the top surface is universal for the shallow filling heights under consideration and is extremely well described by an error function. Next we show that all 22 calculated surface flows may be quantitatively normalized to an error function of the form

$$\omega(\lambda) = \frac{1}{2} + \frac{1}{2}\mathrm{erf}(\lambda), \quad \text{for} \quad \lambda = \frac{r - R_c}{W}, \qquad [5]$$

where R_c is the shear-zone center and W is the shear-zone width. Fig. 2*A* shows ω vs. λ for all 22 simulations along with Eq. **5** plotted in green, and the quality of the normalization is excellent (within 0.01 absolute error, Fig. S3).

The surface flows are well characterized by their shear-zone center R_c and width W. Fig. 2*A*, *Inset* shows that the model adequately captures the dependence of R_c on filling height and its relative insensitivity to d. The experiments are characterized by a power law (5): $(R_s - R_c)/R_s = (H/R_s)^{5/2}$. The relation between W and H is strongly particle-size dependent, and model predictions are in excellent agreement with experiments, per Fig. 2*B*, where $d = 0.35$, 0.8, 1.2, and 2.2 mm from bottom to top. When normalizing by d, as in Fig. 2*B*, *Inset* (plotted in log-log), the model clearly captures the nondiffusive scaling evident in the experimental data, which appears roughly like a 2/3 power law as previously suggested (5). Further results for shallow layers, including the steady-state torque and subsurface shear bands, are included in *SI Text* and Figs. S4 and S5.

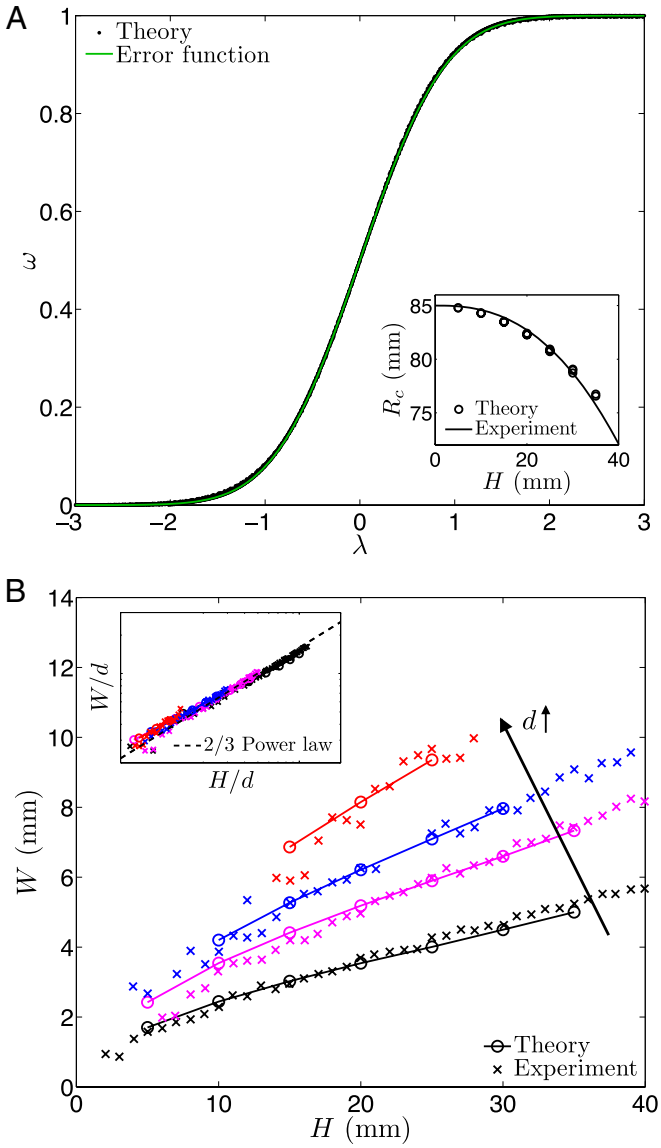

Fig. 2. Comparison of theory and experimental results (5) for shallow layers in the split-bottom geometry. (*A*) For 22 different combinations of *H* and *d*, the surface flow profiles normalize extremely well onto an apparent error function. (*Inset*) Comparisons of the location of shear-band center R_c. (*B*) Shear-band width *W* vs. *H* for $d = 0.35$, 0.8, 1.2, and 2.2 mm, bottom to top. (*Inset*) (log-log) Normalized by *d*. A 2/3 power-law is plotted for reference.

Flows in the Split-Bottom Geometry—Deep Layers. For deeper layers, as R_c moves farther inward, the symmetry of the universal surface flow profile is broken. To examine this transition in our simulations, we match conditions to the corresponding experiments (6), where $R_i = 0$ (i.e., no inner wall), $R_o = 105$ mm, and $d = 1.2$ mm. [We note that Fenistein et al. (6) report a grain size of $d = 0.8$ mm; however, that would make the data reported in ref. 6 inconsistent with their previously reported data (5). Thus, we take $d = 1.2$ mm, which is consistent with the previously reported data.] We consider $R_s = 95$ mm with *H* ranging from 48 to 78 mm and $R_s = 65$ mm with *H* ranging from 40 to 52 mm. The calculated flow profiles for $R_s = 95$ mm and $H = 58$, 68, and 78 mm are shown in Fig. 3 *A*, *B*, and *C*, respectively. As pictured in Fig. 3*A*, shallower layers display the previous shallow flow phenomena, i.e., a shear band terminating at the top surface. However, as *H* increases (Fig. 3 *B* and *C*) a gradual transition takes place, leading to a flow characterized by a quasi-stationary central dome. The transition can be quantified through the rotation of the top center point, $\omega_p \equiv \omega(r = 0, z = H)$. Our model prediction gives an excellent match to the experimentally observed dependence of ω_p on *H*, as in Fig. 3*D*, for multiple values of R_s. (For a comparison of surface flows, see Fig. S6.)

Annular Shear Flow. Whereas a significant degree of geometric variation exists among the family of split-bottom cells, the point that the model is geometrically general and predictive is made more clear by comparing it to flows of glass beads in different families of geometries without adjusting the parameter *A*. As a first validation test, we consider 3D annular shear flow, pictured schematically in Fig. 4*A*, *Inset*. The annular cell has rough walls at inner radius R_i and outer radius R_o, an open top at height *H*, and a perfectly smooth floor. The inner wall is rotated at a rate Ω, giving rise to a wall-located shear band. In keeping with the configuration used in the 3D annular shear flow experiments of Losert et al. (8), we take $R_i = 51$ mm, $R_o = 63$ mm, and $d = 0.75$ mm. We also take $H = 10$ mm (although this geometrical parameter has no

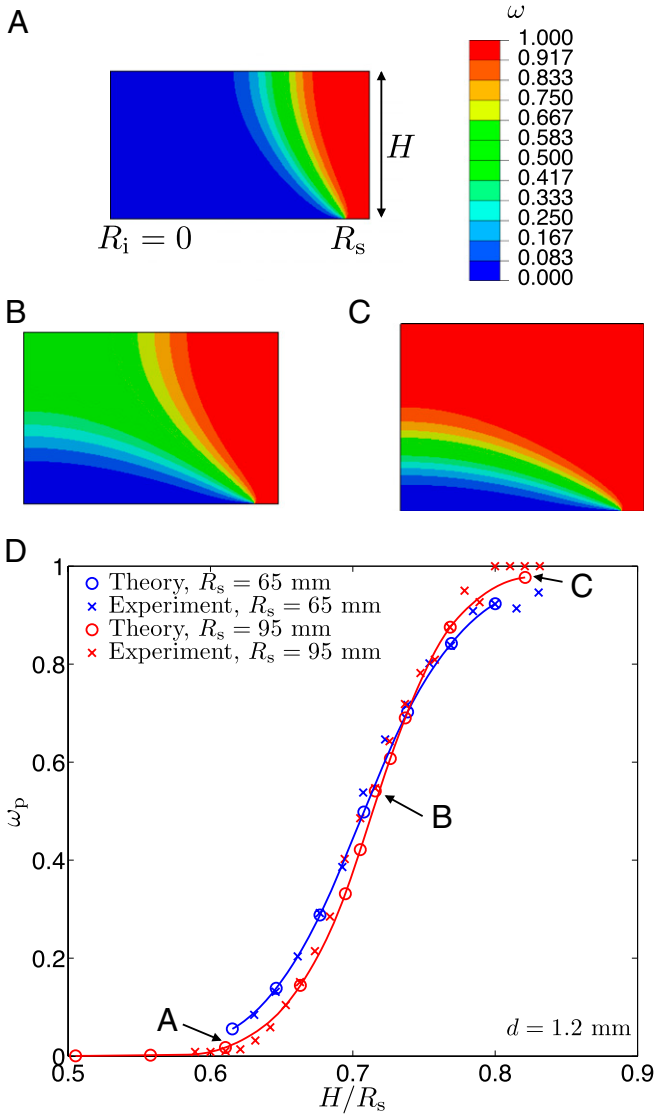

Fig. 3. Comparison of theory and experimental results (6) for deep layers in the split-bottom geometry. (*A*–*C*) Theoretical flow profiles in the *r*-*z* plane for (*A*) $H = 58$ mm, (*B*) $H = 68$ mm, and (*C*) $H = 78$ mm with no inner wall ($R_i = 0$), $R_s = 95$ mm, and $d = 1.2$ mm. (*D*) Variation of $\omega_p \equiv \omega(r = 0, z = H)$ with H/R_s quantitatively predicted by the nonlocal model for $R_s = 65$ mm and $R_s = 95$ mm.

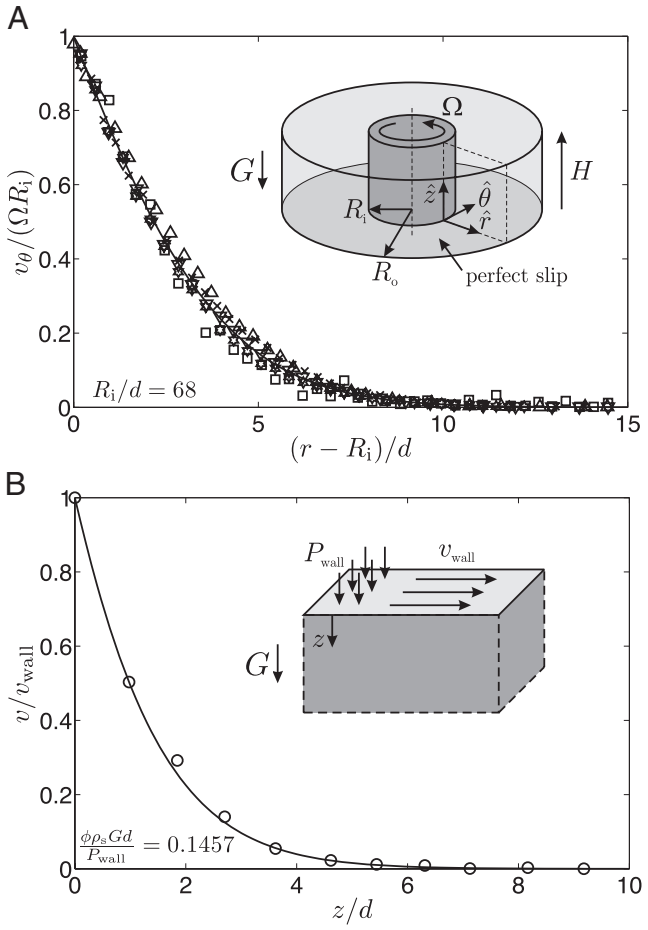

Fig. 4. Comparison of theory and experimental results (8, 10) in other geometries. (*A* and *B*) Theory (solid line) vs. experiments (symbols) for 3D flows in (*A*) annular shear flow with $R_\mathrm{i}/d = 68$ and (*B*) shear flow with gravity present with $\phi\rho_\mathrm{s}Gd/P_\mathrm{wall} = 0.1457$.

observable effect on the simulated surface flow) and $\Omega = 0.16$ rad/s. The value of the outer radius R_o is large enough not to affect the result, but the dimensionless quantity $R_\mathrm{i}/d = 68$ is important in determining the width of the wall-located shear band. The comparison of the model's steady-state prediction along the top surface ($z = H$) to experimental data (8) is shown in Fig. 4*A*. We plot the tangential velocity v_θ normalized by the inner wall speed ΩR_i as a function of the normalized distance from the inner wall, $(r - R_\mathrm{i})/d$. The experimental results represent a variety of inner wall speeds (note the near rate-independent response).

Linear Shear Flow with Gravity. As a final validation test, we consider the flow under a plate being dragged over a bed of gravitationally loaded material, shown schematically in Fig. 4*B*, *Inset*. The rough plate sits atop the bed, imparting a pressure of P_wall (due to the weight of the plate), and is dragged tangential to the top surface at a velocity v_wall, driving shear flow. The bed is much deeper than the grain size d. Due to the gravity-induced pressure gradient in the z-direction, a shear band develops immediately below the plate, decaying into the bulk. In keeping with the parameters used in the plate-dragging experiment of Siavoshi et al. (10), we take $P_\mathrm{wall} = 102.3$ Pa and $d = 1$ mm so that $\phi\rho_\mathrm{s}Gd/P_\mathrm{wall} = 0.1457$. The wall velocity is $v_\mathrm{wall} = 0.3$ mm/s. Further simulation details may be found in *Materials and Methods*. A comparison of the flow prediction of the model to the experimental data (10) is shown in Fig. 4*B*. We plot the horizontal velocity v normalized by the wall velocity v_wall against the normalized coordinate beneath the plate z/d.

Conclusion

We have proposed a simple, size-dependent, continuum-level, 3D constitutive theory for well-developed, dense granular flows. Central to the theory is the granular fluidity, an inverse viscosity scaled by the pressure, which obeys a diffusive differential relation. The microscopic basis of the model relates to the notion that "flow induces flow"; i.e., plastic rearrangements cause stress fluctuations that can induce plastic events in neighboring material. The model has been implemented in a commercial finite-element program (41), and with one experimentally measured material parameter, the nonlocal model quantitatively predicts hundreds of experimental flows in completely different geometries without adjustment, including all salient features of split-bottom flow.

One major assumption of the model is that steady flow progresses at constant volume. This assumption is exactly satisfied in each of the flows considered in the present work, as well as other common settings such as chutes and heap flow. For flow geometries such as silos, hoppers, and rotating drums, the flow field is steady from an Eulerian perspective, but Lagrangian material elements experience changes in the flow rate as they move through the steady Eulerian field. However, flow data in many silo geometries (34) show a rapid approach to the critical packing fraction, such that $\phi = \phi(I)$ is well satisfied throughout. Moreover, other steady rheological approaches, making the same constant volume assumption, have found success in describing silo flows (18, 49), and therefore we fully expect our geometrically general model to be applicable to these technologically relevant flow configurations as well.

There remain several avenues for refinement. Although our theory can model developing flows, it has not been designed to be quantitatively predictive in this regard; fully describing developing or unsteady flows, including shear strengthening/weakening and the effect of the initial state, requires the addition of a critical-state-like model (11). It remains to be seen whether critical-state effects may be incorporated entirely into the local response or whether the fluidity relation in unsteady flows has a separate dynamic term; i.e., a term proportional to $\dot{g}$ in Eq. **3**.

To eventually extend our model to other amorphous materials, a justification based on first-principles continuum thermomechanics is desired. Our belief is that nonlocal effects, through g, give a micoscopic source for power expenditure and that the differential relation Eq. **3** is a microforce balance obtainable from a virtual power argument.

A clearer microscopic understanding of the fluidity boundary conditions accompanying Eq. **3** is needed. Applying our model to flows down rough inclined surfaces will likely elucidate the role of the fluidity boundary condition. It is well known that flows of thin layers of grains down an inclined surface exhibit a size effect whereby thinner layers require more tilt to begin flowing (50), and it is possible that the nonlocal fluidity approach justifies this behavior as a consequence of the lower boundary condition. Approaches based on kinetic theory have had success attributing this phenomenon to the effect of the bottom wall (27), which is encouraging.

Finally, our 3D theory is built upon the common assumption of "codirectionality," which is the most straightforward generalization to three dimensions. This assumption embodies two components: (*i*) The strain-rate deviator and stress deviator tensors are coaxial (share principal directions) and (*ii*) the ratios of their principal values are equal. DEM simulations have observed slight deviations from both of these assumptions, namely ~5% noncoaxiality (45) and the small "normal stress differences" (43). A next iteration of the model would account for these effects.

In closing, we point out the benefits of using an upscaled continuum approach like the one presented herein. We expect significant improvements in computation time to be achieved by using such a method compared with discrete particle approaches. As such, it should provide a useful and expeditious tool in geotechnical design and industrial applications where granular flow modeling on large space scales is required.

Materials and Methods

Finite-Element Implementation. We use the Abaqus finite-element software package (41) and its User Element (UEL) subroutine capability as a tool for solving general boundary-value problems. The governing equations are the equations of stress equilibrium and the nonlocal fluidity relation (Eq. **3**), which are first cast in the corresponding weak form. The nodal solution variables are taken to be the displacements and granular fluidity, which are interpolated inside each element. Using a standard Galerkin approach, a set of element-level residuals may be derived. The system of coupled, nonlinear equations is solved iteratively via a Newton–Raphson procedure, using the Abaqus/Standard solver. We have developed a 3D, linear, eight-noded continuum brick user element for the coupled problem. Explicit details of the weak form and finite-element discretization are found in *SI Text*.

Simulation Details for Annular Cells. Here we discuss the details of our finite-element simulations in annular cells, including all split-bottom geometries as well as annular shear. Regarding displacement boundary conditions, on the side walls, the displacements in the r- and θ-directions are prescribed to match the given wall motion. For the split-bottom simulations, the r- and θ-displacements are also prescribed on the floor of the cell, whereas for the case of annular shear, these degrees of freedom are left unprescribed. In all cases, material may slide without resistance up and down the walls, but the displacement in the z-direction is zero on the floor. The top surface is set to be traction-free. Because flow, stress, and fluidity are symmetric in the θ-direction, the behavior as seen in a downward cut through the annular trough represents the global behavior. A narrow section of the annulus (total angle 0.1°) is simulated using periodic boundary conditions on the front and back faces—nodal displacements on the front face are constrained to be identical to those on the back face except rotated appropriately by 0.1° and nodal fluidities on the front face are constrained to be identical to those on the back face. The section is modeled using a mesh resolution of $0.25d$ in the r-z direction and a thickness of one element in the θ-direction. This resolution was confirmed to produce mesh-independent simulation results. We are interested only in the steady-state flow profiles. To ensure that the steady state is attained, we run the simulations to a final outer section rotation angle of 4°. At this point, no variation is observed in the flow field, and the applied torque has reached a constant value. Further simulation details for the split-bottom cell may be found in *SI Text*.

Simulation Details for Linear Shear with Gravity. We consider a single column of 100 elements in the z-direction, applying the constraint that both the displacements and the fluidity be functions of only z. The column depth is taken to be 10 mm (larger depths produce identical results), and the bottom nodes are fixed whereas the wall velocity is prescribed to the top nodes. The simulation is run to a final lateral displacement of 10 mm to ensure that the flow reaches steady state.

ACKNOWLEDGMENTS. Discussions with Martin van Hecke are gratefully acknowledged. This work was supported by funds from the Massachusetts Institute of Technology Department of Mechanical Engineering.

1. Richard P, Nicodemi M, Delannay R, Ribière P, Bideau D (2005) Slow relaxation and compaction of granular systems. *Nat Mater* 4(2):121–128.
2. Nedderman RM, Laohakul C (1980) The thickness of the shear zone of flowing granular materials. *Powder Technol* 25(1):91–100.
3. Mueth DM, et al. (2000) Signatures of granular microstructure in dense shear flows. *Nature* 406(6794):385–389.
4. Fenistein D, Van Hecke M (2003) Kinematics: Wide shear zones in granular bulk flow. *Nature* 425(6955):256.
5. Fenistein D, van de Meent JW, van Hecke M (2004) Universal and wide shear zones in granular bulk flow. *Phys Rev Lett* 92(9):094301.
6. Fenistein D, van de Meent JW, van Hecke M (2006) Core precession and global modes in granular bulk flow. *Phys Rev Lett* 96(11):118001.
7. Cheng X, et al. (2006) Three-dimensional shear in granular flow. *Phys Rev Lett* 96(3): 038001.
8. Losert W, Bocquet L, Lubensky TC, Gollub JP (2000) Particle dynamics in sheared granular matter. *Phys Rev Lett* 85(7):1428–1431.
9. Midi GDR; GDR MiDi (2004) On dense granular flows. *Eur Phys J E Soft Matter* 14(4): 341–365.
10. Siavoshi S, Orpe AV, Kudrolli A (2006) Friction of a slider on a granular layer: Nonmonotonic thickness dependence and effect of boundary conditions. *Phys Rev E Stat Nonlin Soft Matter Phys* 73(1 Pt 1):010301.
11. Schoefield A, Wroth P (1968) *Critical State Soil Mechanics* (Pergamon, Oxford).
12. Nedderman RM (1992) *Statics and Kinematics of Granular Materials* (Cambridge Univ Press, Cambridge, UK).
13. Jaeger HM, Nagel SR, Behringer RP (1996) Granular solids, liquids, and gases. *Rev Mod Phys* 68:1259–1273.
14. Halsey T, Mehta A, eds (2002) *Challenges in Granular Physics* (World Scientific, River Edge, NJ).
15. Bagnold RA (1954) Experiments on a gravity-free dispersion of large solid spheres in a Newtonian fluid under shear. *Proc R Soc Lond A Math Phys Sci* 225:49–63.
16. da Cruz F, Emam S, Prochnow M, Roux J-N, Chevoir F (2005) Rheophysics of dense granular materials: Discrete simulation of plane shear flows. *Phys Rev E Stat Nonlin Soft Matter Phys* 72(2 Pt 1):021309.
17. Jop P, Forterre Y, Pouliquen O (2006) A constitutive law for dense granular flows. *Nature* 441(7094):727–730.
18. Kamrin K (2010) Nonlinear elasto-plastic model for dense granular flow. *Int J Plast* 26: 167–188.
19. Koval G, Roux J-N, Corfdir A, Chevoir F (2009) Annular shear of cohesionless granular materials: from the inertial to quasistatic regime. *Phys Rev E Stat Nonlin Soft Matter Phys* 79(2 Pt 1):021306.
20. Jop P (2008) Hydrodynamic modeling of granular flows in a modified Couette cell. *Phys Rev E Stat Nonlin Soft Matter Phys* 77(3 Pt 1):032301.
21. Kamrin K, Koval G (2012) Nonlocal constitutive relation for steady granular flow. *Phys Rev Lett* 108(17):178301.
22. Komatsu TS, Inagaki S, Nakagawa N, Nasuno S (2001) Creep motion in a granular pile exhibiting steady surface flow. *Phys Rev Lett* 86(9):1757–1760.
23. Pouliquen O, Forterre Y (2009) A non-local rheology for dense granular flows. *Philos Transact A Math Phys Eng Sci* 367(1909):5091–5107.
24. Aranson IS, Tsimring LS (2002) Continuum theory of partially fluidized granular flows. *Phys Rev E Stat Nonlin Soft Matter Phys* 65(6 Pt 1):061303.
25. Mohan LS, Rao KK, Nott PR (2002) A frictional Cosserat model for the slow shearing of granular materials. *J Fluid Mech* 457:377–409.
26. Savage SB (1998) Analyses of slow high-concentration flows of granular materials. *J Fluid Mech* 377:1–26.
27. Jenkins JT, Berzi D (2010) Dense inclined flows of inelastic spheres: Tests of an extension of kinetic theory. *Granul Matter* 12(2):151–158.
28. Kamrin K, Bazant MZ (2007) Stochastic flow rule for granular materials. *Phys Rev E Stat Nonlin Soft Matter Phys* 75(4 Pt 1):041301.
29. Litwiniszyn J (1963) The model of a random walk of particles adapted to researches on problems of mechanics of loose media. *Bull Acad Polon Sci* 11:61–70.
30. Mullins WW (1972) Stochastic theory of particle flow under gravity. *J Appl Phys* 43: 665–678.
31. Bocquet L, Colin A, Ajdari A (2009) Kinetic theory of plastic flow in soft glassy materials. *Phys Rev Lett* 103(3):036001.
32. Goyon J, Colin A, Ovarlez G, Ajdari A, Bocquet L (2008) Spatial cooperativity in soft glassy flows. *Nature* 454(7200):84–87.
33. Katgert G, Tighe BP, Möbius ME, van Hecke M (2010) Couette flow of two-dimensional foams. *Europhys Lett* 90(5):54002.
34. Rycroft CH, Kamrin K, Bazant MZ (2009) Assessing continuum postulates in simulations of granular flow. *J Mech Phys Solids* 57:828–839.
35. Sollich P, Lequeux F, Hébraud P, Cates M (1997) Rheology of soft glassy materials. *Phys Rev Lett* 78:2020–2023.
36. Dahmen KA, Ben-Zion Y, Uhl JT (2009) Micromechanical model for deformation in solids with universal predictions for stress-strain curves and slip avalanches. *Phys Rev Lett* 102(17):175501.
37. Dahmen KA, Ben-Zion Y, Uhl JT (2011) A simple analytic theory for the statistics of avalanches in sheared granular materials. *Nat Phys* 7:554–557.
38. Picard G, Ajdari A, Lequeux F, Bocquet L (2005) Slow flows of yield stress fluids: Complex spatiotemporal behavior within a simple elastoplastic model. *Phys Rev E Stat Nonlin Soft Matter Phys* 71(1 Pt 1):010501.
39. Lois G, Carlson JM (2007) Force networks and the dynamic approach to jamming in sheared granular media. *Europhys Lett* 80(5):58001.
40. Lemaître A, Caroli C (2009) Rate-dependent avalanche size in athermally sheared amorphous solids. *Phys Rev Lett* 103(6):065501.
41. Abaqus (2010) *Abaqus Reference Manuals, Version 6.10* (Dassault Systèmes Simulia, Providence, RI).
42. Unger T, Török J, Kertész J, Wolf DE (2004) Shear band formation in granular media as a variational problem. *Phys Rev Lett* 92(21):214301.
43. Depken M, Lechman JB, van Hecke M, van Saarloos W, Grest GS (2007) Stresses in smooth flows of dense granular media. *Europhys Lett* 78:58001.
44. Török J, Unger T, Kertész J, Wolf DE (2007) Shear zones in granular materials: Optimization in a self-organized random potential. *Phys Rev E Stat Nonlin Soft Matter Phys* 75(1 Pt 1):011305.
45. Luding S (2008) The effect of friction on wide shear bands. *Particul Sci Technol* 26: 33–42.
46. Sakaie K, Fenistein D, Carroll TJ, van Hecke M, Umbanhowar P (2008) MR imaging of Reynolds dilatancy in the bulk of smooth granular flows. *Europhys Lett* 84(3):38001.
47. Dijksman JA, van Hecke M (2010) Granular flows in split-bottom geometries. *Soft Matter* 6:2901–2907.
48. Jop P, Forterre Y, Pouliquen O (2005) Crucial role of sidewalls in granular surface flows: Consequences for the rheology. *J Fluid Mech* 541:167–192.
49. Staron L, Lagrée P-Y, Popinet S (2012) The granular silo as a continuum plastic flow: The hour-glass vs the clepsydra. *Phys Fluids* 24:103301.
50. Pouliquen P (1999) Scaling laws in granular flows down rough inclined planes. *Phys Fluids* 11:542–548.